Research Article Vol. 12, No. 5 / May 2024 / *Photonics Research* 1055

PHOTONICS Research

Highly efficient fiber to Si waveguide free-form coupler for foundry-scale silicon photonics

Luigi Ranno,[1] **Jia Xu Brian Sia,**[1,2] **Cosmin Popescu,**[1] **Drew Weninger,**[1] **Samuel Serna,**[1,3] **Shaoliang Yu,**[4] **Lionel C. Kimerling,**[1] **Anuradha Agarwal,**[5] **Tian Gu,**[1,5] **and Juejun Hu**[1,5,*]

[1] *Department of Materials Science & Engineering, Massachusetts Institute of Technology, Cambridge, Massachusetts 02139, USA*
[2] *Centre for Micro- & Nano-Electronics (CMNE), Nanyang Technological University, Singapore 639798, Singapore*
[3] *Department of Physics, Photonics and Optical Engineering, Bridgewater State University, Bridgewater, Massachusetts 02324, USA*
[4] *Zhejiang Laboratory, Hangzhou 311100, China*
[5] *Materials Research Laboratory, Massachusetts Institute of Technology, Cambridge, Massachusetts 02139, USA*
**Corresponding author: hujuejun@mit.edu*

Received 13 December 2023; revised 24 February 2024; accepted 17 March 2024; posted 18 March 2024 (Doc. ID 514999); published 1 May 2024

As silicon photonics transitions from research to commercial deployment, packaging solutions that efficiently couple light into highly compact and functional sub-micrometer silicon waveguides are imperative but remain challenging. The 220 nm silicon-on-insulator (SOI) platform, poised to enable large-scale integration, is the most widely adopted by foundries, resulting in established fabrication processes and extensive photonic component libraries. The development of a highly efficient, scalable, and broadband coupling scheme for this platform is therefore of paramount importance. Leveraging two-photon polymerization (TPP) and a deterministic free-form micro-optics design methodology based on the Fermat's principle, this work demonstrates an ultra-efficient and broadband 3-D coupler interface between standard SMF-28 single-mode fibers and silicon waveguides on the 220 nm SOI platform. The coupler achieves a low coupling loss of 0.8 dB for the fundamental TE mode, along with 1 dB bandwidth exceeding 180 nm. The broadband operation enables diverse bandwidth-driven applications ranging from communications to spectroscopy. Furthermore, the 3-D free-form coupler also enables large tolerance to fiber misalignments and manufacturing variability, thereby relaxing packaging requirements toward cost reduction capitalizing on standard electronic packaging process flows.

https://doi.org/10.1364/PRJ.514999

1. INTRODUCTION

Driven by inherent advantages in highly scalable manufacturing [1,2], silicon photonics is a disruptive technology that has influenced multiple application spheres such as quantum optics [3], neuromorphic computing [4,5], optical communications [6], spectroscopy, and sensing [7]. By virtue of the high-index contrast between silicon and its SiO_2 cladding ($\Delta n \sim 2$), dense integration has been enabled by the platform [8]. Active functionalities have also been implemented taking advantage of the high thermo-optic coefficient of silicon [9], its high-speed carrier modulation ability [2,10,11], and monolithic integration with fast and efficient germanium-based photodetectors [12]. In addition, leveraging the established CMOS fabrication processes already developed for the electronics industry, silicon stands as the unrivaled champion in the photonics space.

In recent years, we have witnessed growing commercial deployment of silicon photonics, owing to the increasing sophistication and functionality of silicon photonics circuits as well as critical advantages in manufacturing scalability [13–16]. However, photonic packaging is progressively becoming a major bottleneck. Custom tools with low throughput and active alignment practices are often demanded for photonic packaging [17]. As a consequence, the process accounts for up to 80% of the total costs of photonic modules. The high cost of photonic packaging is mostly attributed to the difficulty of coupling light into and out of the photonic circuit. That comes as a result of the large modal field mismatch between high-index-contrast waveguides and optical fibers, which presents a major barrier for implementation of high-throughput, low-loss coupling schemes [18,19]. Conventional methods involving either edge or grating coupling have their respective limitations [18,19]. For instance, edge couplers (i) can only be placed at the rather limited chip shoreline, preventing full utilization of the chip area and imposing severe design constraints (e.g., on positioning of contact pads); (ii) are difficult to test at the wafer scale, although some solutions have been proposed [20,21], and (iii) generally require sub-micrometer alignment tolerances that are not compatible with passive alignment approaches [19,22]. Grating couplers, on the other hand, are generally not as efficient and show strong wavelength dependence [19,23] due to the inherent wavelength sensitivity of optical diffraction. From a broader perspective, the prevailing I/O issue could potentially infringe upon the competitive advantage of photonic systems, since high coupling losses can escalate the photonic link power budget and overall energy consumption of the entire system. As a result, solving the photonic packaging bottleneck remains one of the most pressing challenges in the field. Overcoming the aforementioned limitations will enable significant cost reduction through leveraging the prevailing electronic packaging infrastructure.

The photonics community has been able to overcome some of the above-mentioned downsides pertaining to the conventional optical coupling approaches. For instance, Tummidi and Webster [24] reported on the use of multiple layers of SiN to form an expanded edge coupler mode capable of achieving coupling loss as low as −0.4 dB when coupling to a standard SMF-28 fiber, while Ding *et al.* [25] demonstrated the use of metal back-reflectors below the Si device layer to produce fully etched, apodized grating couplers with a coupling loss of ∼0.6 dB and 3 dB bandwidth of 70 nm. These solutions nonetheless require processing steps and unconventional material stacks which are not currently available at photonic foundries [1,2,26]. Typically, photonic foundries offer edge couplers with insertion losses of the order of 1.5 dB when coupled with a lensed fiber with a mode field diameter of 3 μm, and grating couplers with coupling losses of approximately −3 dB and 1 dB bandwidth of the order of 30 nm [1,2], still a far cry from the state-of-the-art. Coupling approaches that deviate minimally from the conventional foundry material stack are essential to ensure facile and rapid technology upscaling.

Recently, two-photon polymerization (TPP) has been proposed as a potential approach to provide efficient coupling strategies for integrated photonics [27–29]. Unlocking the third geometric dimension as an additional degree of freedom allows TPP to uniquely produce intricate 3-D designs with submicrometer alignment accuracy, while being compatible with backend integration after the wafer fabrication has been completed. In addition, TPP-written structures have conferred optomechanical alignment benefits during photonic assembly [30–33]. Pioneering work has validated TPP as a viable technique with increasing commercial deployment for robust and versatile photonic packaging [34], having demonstrated optical coupling of waveguides to other waveguides [35–37], lasers [38], free-space [39,40], and fibers [27]. As an example, Lindenmann achieved coupling losses of approximately −4 dB using photonic wire bonding to link a waveguide to a single-mode fiber [41] and −1.7 dB to a multicore fiber [42]. Luo and co-authors reported structures capable of achieving less than 1 dB insertion loss when coupling to single-mode or multicore fibers [43,44]. One limitation of these demonstrations is that they all involve a mode transformer transitioning from an uncladded on-chip waveguide to a low-index-contrast polymer waveguide section prior to coupling to the fiber to mitigate the mode size mismatch. The need for an exposed waveguide section without top cladding nonetheless entails an additional cladding strip process which is often nonstandard in foundry manufacturing and elevates risks of contamination and performance degradation.

Harnessing the TPP technique [28], this work proposes a solution to the photonic packaging bottleneck. Our prior work has involved the demonstration of free-form couplers for SiN waveguides [45]. This work aims to significantly advance the concept by demonstrating efficient coupling from fibers to tightly confined, high-index-contrast Si waveguides using the free-form couplers. Si waveguide coupling incurs a significant technical barrier given the considerably larger mode size mismatch between the Si waveguide and a standard flat-cut (i.e., nonlensed) fiber, which not only compromises the coupling efficiency but also makes broadband and polarization-agnostic operation challenging.

This work addresses several salient aspects with regards to the scalable chip-to-fiber coupling of light for Si waveguides. (1) A highly efficient free-form coupler for foundry-manufactured Si waveguides has been demonstrated (35 μm × 70 μm) using free-form micro-optics enabled by TPP, with coupling losses as low as 0.8 dB. We note that the size of the reflector section can be further reduced (∼35 μm × 30 μm) by trimming it to the divergence angles from the Si facet [Fig. 1(a)] without incurring additional losses. While the coupler is designed for the fundamental TE mode, efficient fundamental TM mode coupling is also shown to be possible where 1 dB bandwidth of 180 nm is demonstrated for TE and 1 dB bandwidth of 130 nm is facilitated for TM. The coupler operates based on optical reflection, designed via the Fermat's principle. While diffraction and refraction exhibit inherent wavelength dependency, optical reflections constitute a chromatically agnostic phenomenon that induces ultra-low optical loss under the total internal reflection (TIR) regime. (2) The Si waveguide to fiber free-form coupler is compatible with cladded waveguides, enabling foundry compatibility. To the best of our knowledge, this aspect has not been addressed thus far among free-form couplers as evident by the abovementioned examples. (3) Different from grating couplers where the fiber is coupled at an angle (i.e., 9°), the fiber is surface-normal in this work. With the growing integration of silicon photonic circuits, there will be an increasing challenge in accommodating the high densities of electrical and optical inputs/outputs (I/O) in a single plane. This situation will be alleviated when the fiber is perfectly vertically coupled to the Si waveguide to fiber free-form coupler. Furthermore, the ability for perfectly vertical fiber coupling implies compatibility with standard alignment tools used in electronic packaging. (4) The free-form coupler is highly resilient to fiber misalignments. This significantly relaxes the precision required for photonic packaging, enabling the application of standard pick-and-place tools and processes from electronic packaging. In addition, the coupler is also tolerant to manufacturing variabilities. (5) The reflector indicates good structural resilience to temperatures as high as 250°C, indicating compatibility with solder reflow [17,46]. (6) The broad bandwidth of the coupler enables far-reaching wavelength diverse applications such as neuromorphic computing [4,5], wavelength-division multiplexing (WDM) communications [47], or spectroscopic sensing [48]. Lastly, we propose an approach that enables the scalable packaging of the reflectors for resilient fiber or fiber array bonding, of relevance for the real-world deployment of this technology.

2. DEVICE CONCEPT AND DESIGN

A. Broadband Reflector Design via the Fermat's Principle

The Si waveguide to fiber 3-D free-form coupler, designed for the fundamental TE mode, is illustrated in Fig. 1(a). The Si taper, deep trench, and reflector sections are indicated. The inverse taper was implemented by virtue of its relatively large output mode size (~3 μm^2), and hence, lower divergence angle as compared to a conventional waveguide. This results in a reduction in the aspect ratio of the reflector while simultaneously facilitating efficient total internal reflection by expanding the reflector size along the light propagation direction. The 3-D free-form coupler [Fig. 1(a), *xyz* coordinates labeled] utilizes the principle of wavefront interference to efficiently couple light between the in-plane Si waveguide mode and an out-of-plane fiber mode oriented orthogonally. To avoid computationally intensive point-by-point local optimization often used for the development of free-form optics [49], we take advantage of the Fermat's principle to vastly simplify the optimization procedure [45]. Considering an arbitrary reflector surface which redirects the light wave exiting a waveguide upward into an optical fiber, the Fermat's principle dictates that the total optical path length traversed by the light wave must be stationary, resulting in the following relation:

$$\phi_1 + \phi_2 = \phi_{\text{total}} = \text{constant}. \tag{1}$$

ϕ_1 and ϕ_2 are the phase delays accumulated by propagating the light wave as it travels from the Si taper to the free-form reflector surface, and from the reflector surface to the fiber facet, respectively. ϕ_{total} must be a constant following the Fermat's principle. In Eq. (1), we neglect the TIR phase delay accumulated upon reflection at the coupler surface since it remains nearly constant for different light trajectories.

Figures 1(b) and 1(c) depict the phase of the propagating light wave, determined through 3-D finite-difference time-domain (FDTD) modeling of the Si taper and optical fiber separately. In Fig. 1(d), we consider co-propagation of forward-propagating light from the Si taper and backward propagation of the light wave output from the fiber [i.e., the time reversal of Fig. 1(c)]. To back propagate the light wave from the fiber, we instead define a wavefront X [Fig. 1(c)] acting as the "light source" from which the light wave propagates upward. ϕ_3 denotes the phase delay from X to the fiber. According to Fig. 1(c), the phase delay due to propagation from the X to a point on the reflector surface is then given by $\phi_3 - \phi_2$. The condition for constructive interference between the light waves exiting from the waveguide and from the "source" X is

$$\phi_1 - (\phi_3 - \phi_2) = \phi_{\text{total}} - \phi_3 = 2N\pi. \tag{2}$$

Since ϕ_3 is identical for all light paths between X and the fiber facet, Eq. (2) implies that $\phi_{\text{total}} = 2N\pi + \phi_3$ is a constant and is equivalent to the stationary optical path condition specified by the Fermat's principle. Therefore, the loci of constructive interference, which are located using a spiral trace search algorithm [45], correspond to a group of reflector surfaces that

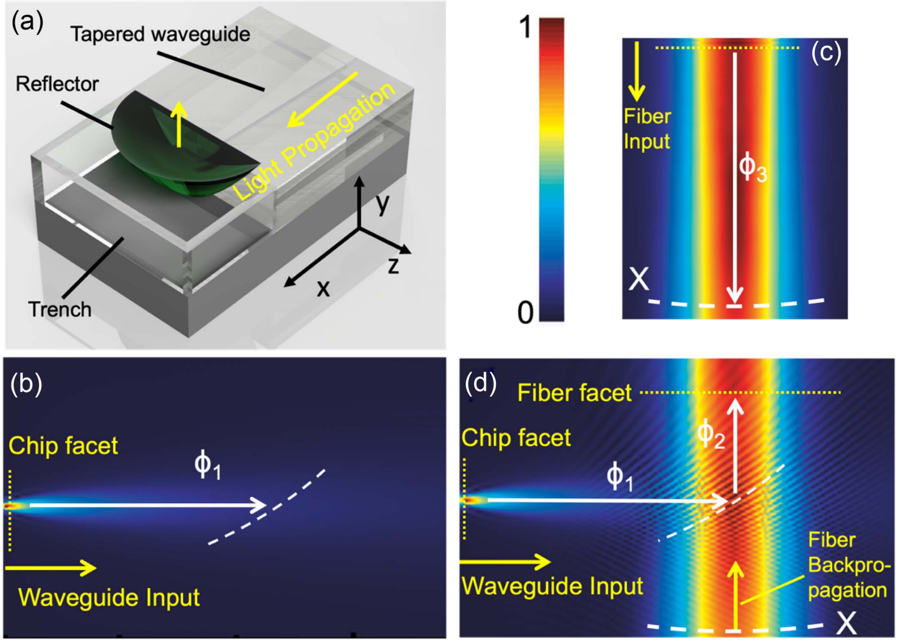

Fig. 1. (a) 3-D schematic of the fiber to Si waveguide free-form coupler. The Si nonlinear inverse taper, deep trench, and reflector sections are annotated. The design methodology of the free-form coupler is guided by the Fermat's principle. 3-D FDTD simulations of (b) forward-propagating light wave exiting from the Si waveguide inverse taper, (c) forward-propagating light wave from the fiber, and (d) co-propagation of back-propagated light wave from the fiber and forward-propagating light from the waveguide taper. The white arrows illustrate the phase accumulated by the light wave as it propagates. The yellow arrows indicate the light sources in the different simulations, and corresponding propagation directions.

fulfill Eq. (1). The optimal surface can be identified by finding the locus yielding highest overlap integral between the two light waves (from the waveguide and X, respectively). Unlike prevailing grating couplers that involve computationally intensive optimization algorithms [26,50], this design approach involves only two full vectorial FDTD simulations, namely forward propagation of the fiber mode in absence of the Si waveguide, and co-propagation of the back-propagated (fiber) wave from X and light exiting from the Si waveguide mode. The optimal reflector surface is selected deterministically without iterative optimization.

The Si waveguide geometry at the taper end facet plays a significant role in determining the shape and efficiency of the coupler [Fig. 1(a)]. Figure 2(a) plots the electric field distribution of the light waves in the *xy* plane as it exits from 170 nm (top) and 480 nm (bottom) wide waveguides. Here the 480 nm width is chosen because it is close to single-mode cutoff at the C-band. The narrower waveguide gives rise to a much lower divergence angle, as illustrated in Fig. 2(a). To that effect, reduction of the divergence angle through appropriate waveguide taper design will minimize loss due to asymmetric intensity distribution of the field reflected from the coupler [51]. It also follows that the minimum size of the reflector is bound by the highest angle at which TIR can be maintained and, given that the refractive index of typical TPP polymers is less than 1.6 [52], shallower structures enabled by tapered waveguides perform better.

The Si nonlinear inverse taper was designed to adiabatically expand the waveguide mode, thereby simultaneously reducing the coupler size and also the far-field divergence angle. Furthermore, the Si nonlinear inverse taper design critically impacts the substrate leakage loss, as the Si waveguides are fabricated on a 220 nm SOI platform with 2 μm thick buried oxide. By imposing a slower width tapering rate at the beginning and faster width change toward the end, the waveguide mode is confined as much as possible along the taper and only expanded at the end to facilitate coupling to the reflector, thereby enabling adiabatic transition with minimal substrate leakage loss. More specifically, the taper narrowing follows an $x^{1.25}$ function in between the two ends, where the exponent was optimized to minimize the total insertion loss of the taper. The length of the taper is 100 μm with an optimized insertion loss of ~0.05 dB at 1550 nm. The electric field distributions of the waveguide mode in the *xy* and *xz* planes are plotted. The nonlinear taper preserves the polarization while expanding the field laterally, hence resulting in a more symmetric mode profile. While the free-form coupler is designed for efficient coupling of the fundamental TE mode, it is anticipated that it can also

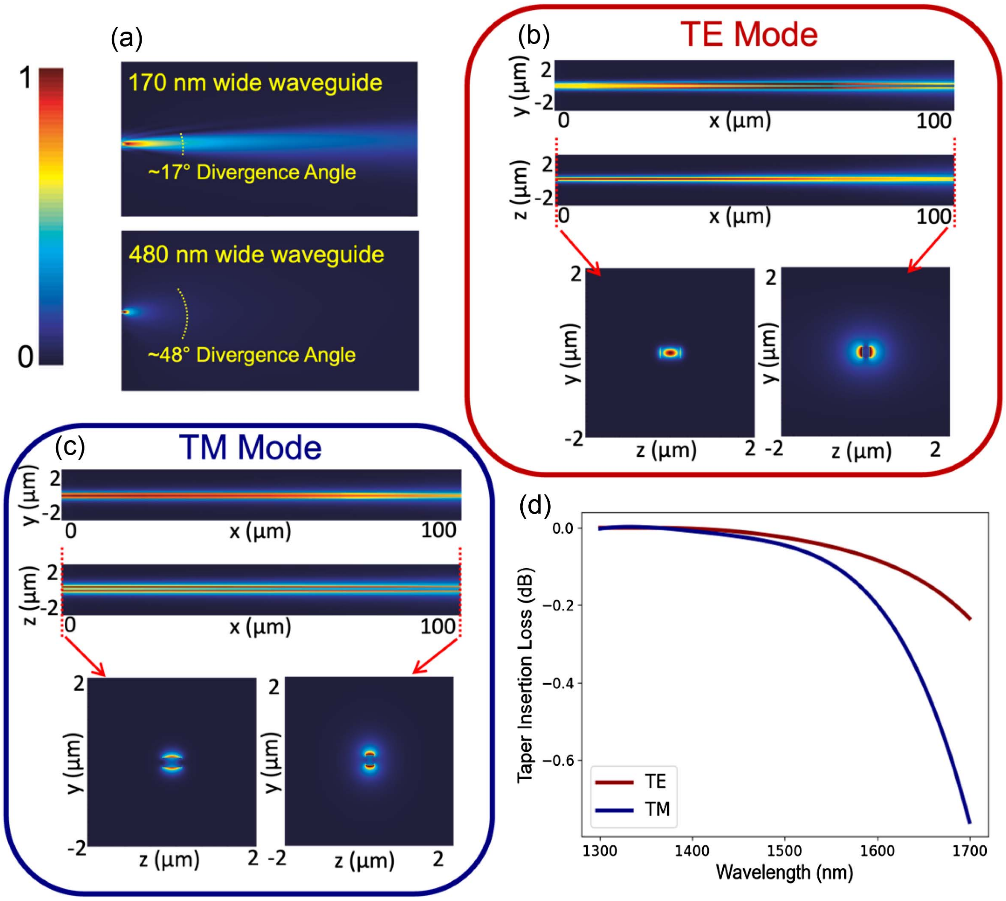

Fig. 2. (a) TE-mode electric field distribution in the *xy* plane of light waves exiting from 170 and 480 nm wide waveguides at 1550 nm wavelength. The full width at half-maximum divergence angles are marked. The electric field intensity of the light waves in the *xy* and *xz* planes as (b) fundamental TE mode and (c) fundamental TM mode propagate along the nonlinear inverse taper. The respective electric field distributions (*yz* plane) at both facets of the taper are shown. (d) Spectral dependence of the total insertion loss of the taper.

operate with the fundamental TM mode. As such, the capability of the nonlinear inverse taper for adiabatic TM mode conversion is also investigated in Fig. 2(c), where low-loss mode conversion and mode spatial preservation are verified. The spectral dependences of the nonlinear inverse taper for both polarizations are considered in Fig. 2(d), showing that the substrate leakage losses dominate at longer wavelengths. The fundamental TM mode shows larger substrate leakage loss as compared to TE, due to the stronger out-of-plane confinement of the TE mode field.

The *xy* section of the free-form coupler is shown in Fig. 3(a). The photonic chip was fabricated at AIM Photonics, whose standard process design kit (PDK) includes etching a deep trench for dicing. Here we leverage the etching step to define the recess in which the reflectors were printed. A false colored scanning electron microscope (SEM) image is shown in Fig. 3(b). The reflectors were fabricated using TPP by polymerizing IP-n162, a commercially available resin from Nanoscribe GmbH boasting low absorption and high TPP resolution. The printing process was carried out using a Photonic Professional GT2 system with an averaged laser power of 60 mW and hatching/slicing distances of 100 and 200 nm, respectively. The exposure of an individual micro-reflector took 157 s. A discussion on methods to improve throughput is presented in Appendix A. Top panels in Fig. 3(d) show the near-field optical intensity distributions for TE polarization at the waveguide end facet, the fiber mode, and the reflected beam. A large field overlap of 92% between the latter two was verified through overlap integral. The beam forming characteristics of the reflector are showcased by plotting *xz* sections of optical intensity distributions at different heights from the reflector surface. For comparison, the near-field distributions with TM-mode input are also shown in Fig. 3(e). For TM polarization, a field overlap of 84% between the reflected beam and the fiber mode is achieved. The spectral performance of the coupler is modeled and plotted in Fig. 3(c) for the fundamental TE mode, where coupling loss as low as 0.5 dB is shown. While the free-form coupler is designed and optimized for the fundamental TE mode, it is found to be also efficient for the fundamental TM mode where minimum coupling loss as low as 0.8 dB (1.3 dB at 1550 nm) is computed. Through simulation, the coupler shows 1 dB bandwidth of over 300 nm in the TE polarization, and 1 dB bandwidth exceeding 200 nm in the TM polarization. The electric field distributions in the *xy* plane are shown in Fig. 3(d) and Fig. 3(e), respectively, for the two polarizations. Even though the coupler is designed for the TE mode it still affords highly efficient coupling for both polarizations compared to the state-of-the-art [1,2,19].

B. Fiber-Coupler Alignment Tolerance Analysis

Tolerance to fiber misalignment is an important metric with regard to photonic packaging, as a more tolerant coupler allows using faster packaging procedures that forego the burden of active alignment and drive down the packaging cost. In

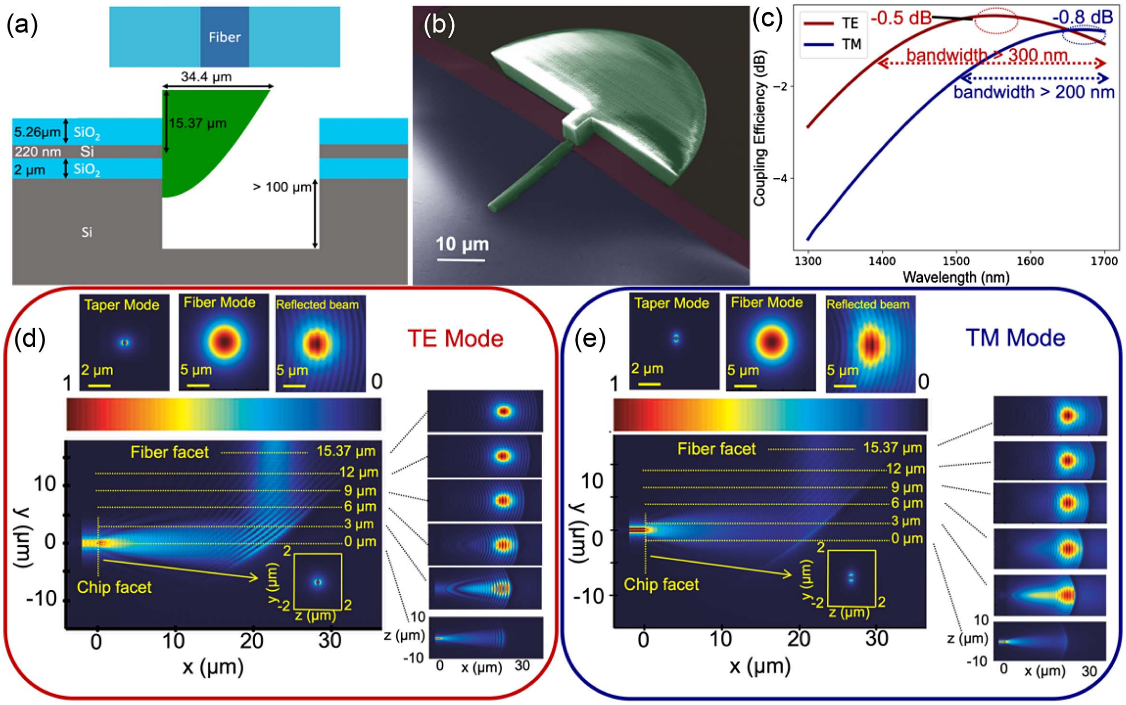

Fig. 3. (a) Cross-sectional illustration of the designed free-form coupler, where the constituent components are illustrated and critical dimensions are labeled. (b) False-colored SEM image of the fabricated free-form coupler. The two slabs (short and thick, and long and thin) extending toward the waveguide are visual aids to quickly gauge alignment accuracy in and out of plane; they do not perform any optical function. (c) Simulated spectral performance of the designed free-form coupler for the case of TE and TM waveguide polarizations. Electric field intensity (*xy* plane) as the light wave is coupled between the fiber and the Si waveguide through the coupler for the case of (d) fundamental TE and (e) TM polarization. The electric field (*xz* plane) evolution of the optical mode as it is reflected normally from the Si waveguide and propagates toward the fiber facet is shown for different *y* positions. The optical modes at the taper, reflector, and fiber output are also illustrated.

Figs. 4(a) and 4(b), the alignment tolerance of the 3-D free-form coupler is investigated through simulations. From Fig. 4(a) it can be seen that the 1 dB alignment tolerance of the coupler with respect to in-plane (*xz*) fiber misalignments is approximately ±2.2 μm, as expected given the beam size closely matching the SMF-28 fiber mode. In addition, the coupler shows remarkable tolerances in the *y* direction, where a spacing as large as 40 μm between the fiber and the coupler leads to an excess loss of only 1 dB, much better than the 10 μm that conventional grating couplers achieve [53]. This can be attributed to the highly collimated beam exiting from the top surface of the coupler. The tolerance to misalignment between the coupler and the waveguide, which can occur during the TPP printing process, is also investigated in Fig. 4(c). The design is highly tolerant to misalignment in the *x* direction whereas ±6.5 μm alignment accuracy is mandated for an excess loss of less than 1 dB. Furthermore, the coupler also shows good resilience to manufacturing tolerance in the *y* and *z* directions, where misalignment of ±0.75 μm leads to an increase in excess loss of 1 dB. These values are well within the alignment accuracy of TPP: printing with misalignment below 200 nm has been experimentally demonstrated [54] and commercial systems capable of automated alignment are already available on the market [55]. The results suggest excellent robustness of the free-form coupler technology against possible alignment errors in both manufacturing and packaging processes.

3. EXPERIMENTAL DATA

The transmission of the 3-D free-form coupler is measured using two flat-cleaved fibers (SMF-28), oriented normal to the chip surface, directed to two couplers located at both ends of a silicon waveguide [Fig. 5(a)], and controlled through the use of piezoelectric motors with an automated stage (SD-100 from Mapleleaf Photonics). As a testament to their wavelength-agnostic performance, Fig. 5(a) demonstrates coupling of visible red light with less than 1 dBm input power to the waveguide so that, despite the significant material losses of silicon, a bright beam output is visible. Three different tunable laser sources (TSL series from Santec) are controlled through the use of an optical switch module (OSU-100), which is connected to the input fiber via a fiber polarization controller (FPC), while the photodetector (MPM-210) is connected to the end of the output fiber. The measured spectral performance of an individual reflector is shown in Fig. 5(b), where the coupling loss is taken as half the total measured insertion loss after subtraction of waveguide propagation loss and system loss. A minimum coupling loss of 0.8 dB with a 1 dB bandwidth in excess of 180 nm was observed for the TE mode. The TM polarization yields a minimum loss of ∼3 dB per facet, with a 1 dB bandwidth larger than 130 nm, despite the fact that the coupler is designed and optimized for the TE polarization. Nonetheless the results still indicate excellent dual polarization coupling capabilities, especially considering that typically TM grating couplers have insertion losses of ∼4–5 dB [56,57]. Most importantly, the experimental results correspond closely to the designed performance, which validates the coupler fabrication process flow. An analysis of the factors contributing to the excess loss observed in experiment as opposed to simulation is provided in Appendix B. To the best of our knowledge the free-form coupler demonstrates one of the best fiber to Si

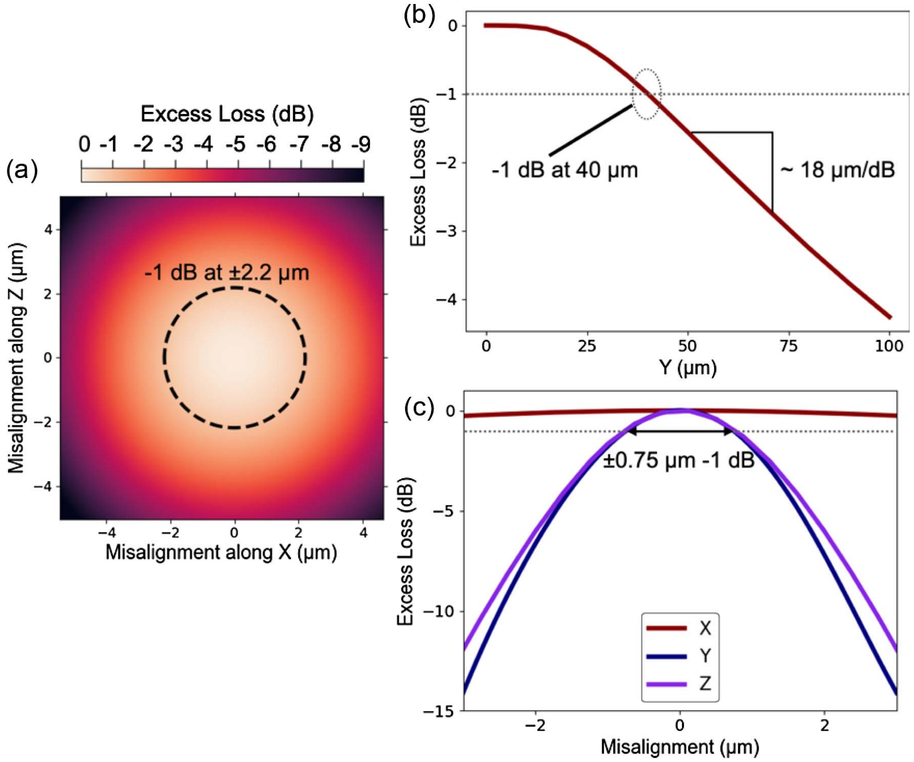

Fig. 4. Computed fiber misalignment tolerance in the (a) *xz* plane and (b) *y* direction. (c) Computed excess loss in coupling efficiency of the reflector as a result of printing misalignments with respect to the waveguide facet. Simulated for TE polarization at 1550 nm.

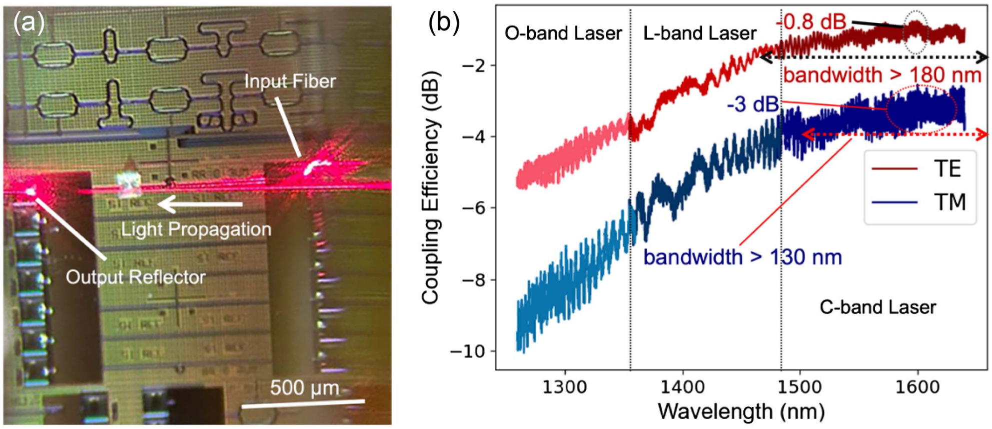

Fig. 5. (a) Micrograph showing fiber-coupled (SMF-28) red laser light (630 nm) into a Si waveguide via the free-form couplers. (b) Measured spectral performance of the 3-D free-form coupler pertaining to the fundamental TE and TM modes.

waveguide coupling performances (coupling loss and bandwidth) based on a foundry-compatible design.

Following the simulations performed in Fig. 4, the fiber misalignment tolerance was measured (Fig. 6) using a piezoelectric actuator with a step size of 500 nm. After determining the optimal position of the input and output fibers, the position of the output fiber was rastered to map the coupling efficiency as a function of the fiber position. The coupler is experimentally verified to enable 1 dB alignment tolerances of ∼ ±2 μm in the *xz* plane [Fig. 6(a)], consistent with simulation results. Furthermore, as expected from the collimated beam formed by the coupler, a large *y* direction [Fig. 6(b)] tolerance is also observed, where a 19 μm misalignment only leads to 1 dB excess loss.

4. DISCUSSION

To demonstrate the advantages of the proposed design, the free-form coupler is compared against a standard foundry-PDK grating coupler [Fig. 7(a)]. The transmission across a Si waveguide configured with grating couplers on both ends, as well as one with a grating and a free-form coupler, was measured using the LUNA OVA 5000 optical vector analyzer and shown in Fig. 7(a). The insertion loss of the setup and waveguide propagation loss were subtracted from the two spectra. The advantages of the 3-D free-form coupler can be clearly expounded. First, ∼2 dB decrease in insertion loss is evident even at the peak efficiency of the gratings. Furthermore, significant broadening of operation bandwidth can be seen. The increase in bandwidth becomes even more apparent when compared to Fig. 5(b), where the couplers are implemented on both ends of a waveguide. This speaks of the superior fiber to chip coupling capabilities of the free-form couplers for potential deployment in next-generation silicon photonic circuits where power consumption is of upmost importance.

In addition to their excellent optical performance, the free-form couplers are also compatible with standard electronic packaging processes. This is in view of (1) the surface-normal (i.e., with zero degree tilt angle) fiber coupling configuration that is compatible with standard electronic packaging tools; (2) the significant tolerance to fiber misalignment (1 dB alignment tolerances of ±2 μm and 19 μm in the *xz* plane and *y* direction, respectively), commensurate with state-of-the-art assembly tools used in electronic packaging [58,59]; and (3) compatibility with the thermal budget of standard packaging

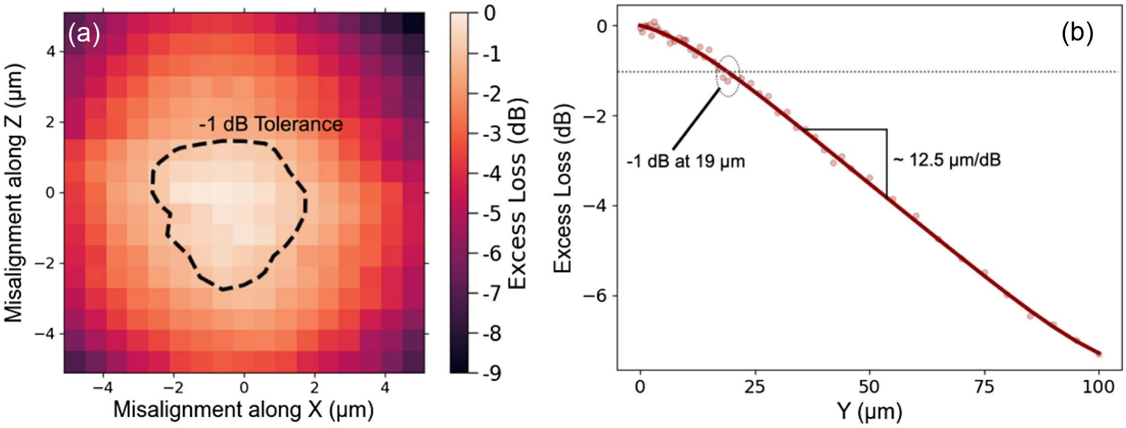

Fig. 6. (a) Measured fiber misalignment tolerance in the *xz* plane measured using a piezoelectric actuator with a step size of 500 nm. The contour traces the 1 dB alignment tolerance. (b) Measured excess loss as a function of output fiber misalignment in the *y* direction.

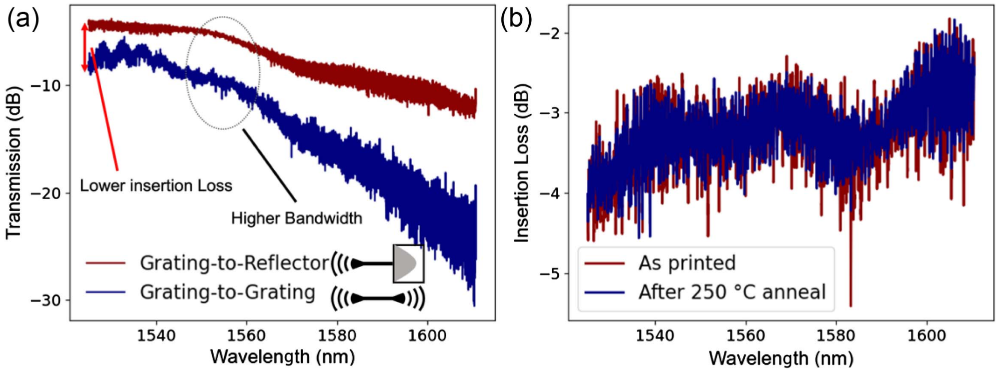

Fig. 7. (a) Measured spectra for two Si waveguides with different configurations of light coupling: grating-to-reflector and grating-to-grating. (b) Measured total insertion loss of a Si waveguide terminated with two free-form couplers as-fabricated and after annealing at 250°C for 10 min.

processes. The last point was validated by comparing the measured spectra of the couplers before and after annealing (250°C) for 10 min in Fig. 7(b). The conditions were chosen to represent the typical heat treatment process used in Pb-free solder reflow [46]. Further, to provide additional evidence of the resilience of the reflectors, changes in their performance upon being subjected to high levels of optical infrared power up to ~450 mW were monitored, with no visibly adverse effect being observed. Details on the study are provided in Appendix C.

In addition to the benefits presented above, the free-form couplers feature a compact footprint and are designed to work with standard foundry-processed cladded waveguides (i.e., do not require a long uncladded or polymer cladded section for mode transition [42–44,60]). This is an important advantage over other proposed TPP couplers enabling high-density optical I/O on “zero-change” foundry-manufactured photonic chips. The coupler can also be combined with TPP-printed optomechanical fixtures to facilitate passive alignment and assembly. Some excellent work done by Gordillo *et al.* [30] showcased the potential of TPP for such purposes, although it was only applied to grating couplers. Similarly, the Bakir research group has investigated various approaches to interconnect fibers and photonic chips (with grating couplers) using etched chips with printed fiber ferrules [31–33]. We propose a potential solution for large-scale packaging of the free-form couplers with fiber arrays. The envisioned structure is illustrated in Fig. 8, both for the case of an individual optical fiber [Fig. 8(a)] and a fiber array [Fig. 8(b)]. After printing of the reflector(s), an additional alignment structure is printed onto the chip top surface, maintaining alignment with the printed reflectors. The alignment structures consist of two components: one guiding sleeve which serves the purpose of guiding the fiber (array) into the position, and a stopper which prevents collision with the reflector top surface and also enables optimal spacing between the fiber facet and reflector top surface. Once the fiber (array) is rested onto the stopper, optical epoxy can be used to bond the assembly together, forming a sturdy package capable of withstanding mechanical vibrations while also isolating the reflectors from the external environment. Printing the bulk of the alignment structure, which does not require high resolution, may take advantage of beam expansion procedures that vastly increase the voxel size (e.g., UpNano’s adaptive resolution function [61]), hence substantially reducing the total printing time. In addition, the lack of overhanging features (both the reflectors and alignment structures) makes the proposed design stand out thanks to its compatibility with nanoimprint/embossing. This convenient and scalable packaging solution differentiates our design from prior arts, opening the door to future implementations at the wafer scale.

5. CONCLUSION

This work demonstrated 3-D free-form couplers that enable highly efficient and broadband coupling between fibers and

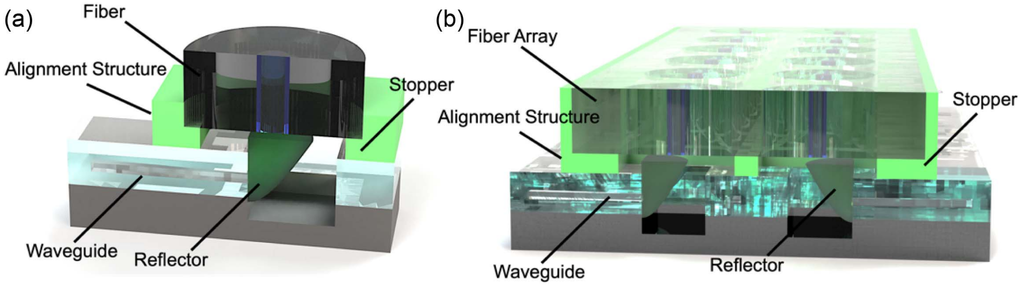

Fig. 8. Potential photonic packaging solution involving the free-form coupler, enabling packaging with (a) individual fibers and (b) fiber arrays. A mechanical alignment feature is printed onto the chip, with a stopper to prevent collision of the fiber (array) with the reflector surface. The fiber (array) is guided by the alignment structure and brought down onto the chip, until it rests onto the stopper. The optical assembly can then be bonded with optical epoxy as is conventionally done for grating couplers.

tightly confined Si waveguides. The 3-D free-form couplers, optimized for the TE mode, lead to a coupling loss down to 0.8 dB in the C-band with a 1 dB bandwidth in excess of 180 nm. In addition, the coupler can also operate with TM polarization with a minimum coupling loss of 3 dB and a 1 dB bandwidth of larger than 130 nm. The free-form couplers also feature significant tolerance against fiber and manufacturing misalignments, thereby relaxing the precision and cost involved in photonic packaging. The coupler design is fully compatible with the standard 220 nm SOI platform without involving custom cladding stripping steps, and is compatible with the thermal budget of solder reflow processes commonly used in electronic/photonic packaging. Furthermore, the micro-reflectors can withstand high optical powers in excess of 450 mW. We envisage this work to provide a viable pathway to resolve the pressing issues related to the packaging bottleneck that silicon photonics is facing.

APPENDIX A

Given the economy of scale that enables the success of the semiconductor industry, it is clear that throughput is an essential parameter to assess the scalability of a solution in the industry. As a result, discussing the speed at which the micro-reflectors are printed, and potential ways in which the throughput could be improved is of great value to the photonics community.

To start, using the printing parameters introduced above (Photonic Professional GT2 printed, 60 mW of averaged laser power, hatching distance of 100 nm, and slicing distance of 200 nm) the print time for one device is 157 s. The printing time can be greatly reduced by (i) truncating the shape of the reflector to the divergence angle of the beam exiting the waveguide, (ii) printing using the "shell and scaffold" mode, or (iii) using more advanced printing modalities such as UpNano's adaptive resolution [61].

The first option, i.e., trimming of the shape, is the easiest to employ and can be readily applied to the structure presented in the work. For instance, a reflector created by trimming the later portions beyond ±12 μm would incur no meaningful loss in performance but could be printed in only 104 s.

Second, the usage of "shell and scaffold" printing, where only the shell of the structures is written by TPP, followed by removal of the excess resin in a developer and then UV flood exposure to polymerize the core of the structure enclosed by the shell, is an attractive solution which brings down the printing time to as low as ∼6 s.

It should also be noted that TPP is evolving rapidly, and newer machines enable much faster printing without sacrificing performance. For instance, Nanoscribe's Quantum X can print optical quality micro-lenses at speeds of 20 mm^2/h for 100 μm thick lenses [62]. In fact, industry has started to implement TPP technology at a small scale and initial investments by packaging houses, e.g., the partnership between PHIX and Nanoscribe [34], is bringing products such as facet-attached micro-optics to a larger user base. Furthermore, in addition to hardware and software improvements, various printing modalities have been proposed to further increase throughput, such as projection-based exposure to parallelize the printing process or using multiple laser beams to expose different areas simultaneously [28]. In addition, structures compatible with nanoimprinting or hot embossing (which includes the micro-reflectors proposed in this work) could be easily upscaled into production by fabricating an initial master mold via TPP which can then be replicated in high volumes [63].

APPENDIX B

Understanding the factors that led to a slight discrepancy in optical performance between the designed and measured micro-reflectors is of key importance to determining areas of improvements for future work. For this purpose, we consider three potential sources of additional loss: (i) material absorption, (ii) scattering induced from surface roughness, and (iii) shape distortion as compared to the designed geometry.

We can estimate that the extinction coefficient of the resin at 1550 nm is of the order of $\sim 10^{-6}$ around 1550 nm, and generally stays low for the entirety of the telecommunications band [45,52]. If we assume an optical path of ∼50 μm (an overestimate given the physical size of the reflectors), then we can expect an absorption loss of the order of 0.002 dB. As a result, even if we assume a slightly higher loss a result of a different degree of polymerization as compared to what is reported in the literature, we can safely neglect the absorption losses of the material as playing a significant role in the device performance.

Second, the surface roughness that can be achieved by the GT2 system, which was used in this work, can be lower than 20 nm [64]. We confirmed that the tool is indeed capable of producing surfaces with such smoothness by scanning the top surface of a printed cube using an atomic force microscope (AFM). The AFM micrograph is presented in Fig. 9(a); the root mean square surface roughness in the area masked in red is 17.6 nm. Given the fact that the surface roughness is considerably lower than the operating wavelength, it can be anticipated that surface roughness does not contribute significantly to the excess loss of the device. With that said, it should also be noted that more recent TPP printers, e.g., Nanoscribe's Quantum X series or UpNano's NanoOne, can achieve significantly lower surface roughness (less than 5 and 10 nm, respectively) through the use of grayscale lithography [62] or better control or the voxel near the outline of the 3D printed structure [65].

Lastly, another potential source of loss is related to shape deformation as a result of material shrinkage, occurring as a result of the density difference between polymerized and unpolymerized resin, or capillary forces encountered during development, among others [66]. Unfortunately, correctly characterizing the 3D shape of printed micro-optics is very challenging since deformations occur as a result of complex dynamics and mechanical constraints (e.g., being attached to a surface as opposed to "free to move"), resulting in regions experiencing vastly different degrees of deformation. Although some approaches have been proposed such as reconstruction through the use of multiple SEM images taken from different points of view or using X-ray computed tomography [28,64], currently there are no tools developed for this application.

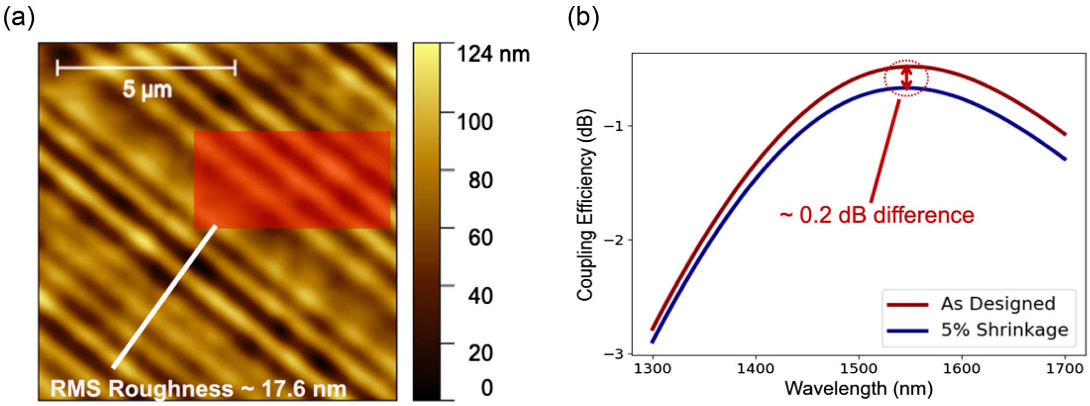

Fig. 9. (a) Atomic force micrograph of the top surface of a printed cube. The striations observed come as a result of the discrete lines exposed during the printing process. The root mean square roughness of the masked area is 17.6 nm. (b) Simulation on the effect of shrinkage on coupling efficiency of the free-form reflector. A uniform 5% shrinkage was applied.

For the case of the free-form reflectors described in this work, given the complex nature of their shape, it is not practical to fully characterize the shape and therefore we investigate the effect of a uniform contraction of 5% on the optical performance, with 5% being an upper bound on the shrinkage that might be typically experienced in TPP. A comparison of the performance of the designed reflector, and the same reflector with 5% uniform shrinkage is presented in Fig. 9(b). As it can be seen, shrinkage tends to reduce the efficiency, with a loss in performance of about 0.2 dB in the proximity of 1550 nm where the reflector performance is the highest. In reality, we expect that the shape deformation will be nonuniform due to the constraints enforced by being attached to the chip facet which will result in lower contraction in the areas closer to the chip facet and higher deformations further away from the facet. As a consequence, these results can be used as evidence on the importance of shape control in order to achieve high-performance micro-optics.

Given the magnitude of this figure, it is likely that the highest contribution to the excess loss observed experimentally is related to shape deformations. This could also explain the minute differences observed in the profiles of the output beam formed by the micro-reflector as compared to the ideal ones (Fig. 4 versus Fig. 6).

As the field matures, we anticipate that 3D metrology tools to characterize the geometry of TPP-printed structures will aid designers in minimizing the effects of shape deformation by preventively applying corrections to the input design files such that the fabricated structure (after the effect of shrinkage) will match the intended design.

APPENDIX C

The ability to tolerate high laser power is a highly desirable property for any optical I/O device, as such requirements are often found in various applications such as nonlinear optics [67], millimeter waves [68], or LiDAR [69]. As a result, testing the resilience of the couplers when exposed to such high powers is of considerable importance. We emphasize that, even though silicon waveguides themselves are limited in the amount of optical power they can generally transmit due to limitations from two-photon absorption processes, confirming the capability to operate in high-power conditions is of perhaps even higher interest for the case in which the couplers are applied to other material platforms, e.g., SiN, AlN, Ta_2O_5, $LiNbO_3/LiTaO_3$, that do not suffer from this limitation.

In order to test the power handling capability of the couplers, the optical link comprising a reflector-grating coupler was measured, once before and once after the reflector had been illuminated with high optical power for 1 h consecutively. First, input and output fibers were aligned to the optical link, placing the input fiber on top of the reflector and the output on top of the grating. Then the system was scanned using the LUNA OVA 5000 optical vector analyzer. Following, the input fiber was connected to a high-power erbium-doped fiber amplifier (EDFA-BA-GF-25-B), whose input was the laser light sourced by an HP 8164A light wave measurement system with emission centered at 1550 nm. The total output power emitted by the

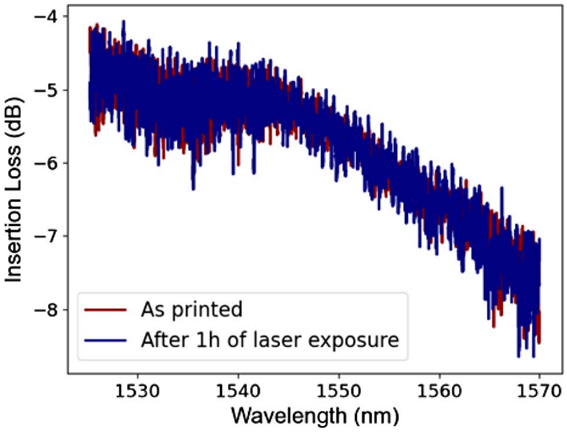

Fig. 10. Optical performance of a photonic link comprised a free-form reflector and a grating coupler as input/output devices, before (red) and after (blue) exposure to ~470 mW of continuous-wave laser emission centered at 1550 nm for 1 h continuously. It can be deduced that little to no change occurred, indicating the compatibility of the reflectors with high-power applications.

EDFA-boosted light source reached ∼470 mW (measured using an optical power meter, Newport 2832-C). After 1 h of continuous exposure to the high-power source, the input was changed back to the LUNA OVA and another scan was performed. The optical spectra showing the performance of the reflector before and after are shown in Fig. 10.

As can be seen, the reflector survived the high-power irradiation without indicating any sign of degradation or loss in performance, at least up to the power levels tested in this experiment. It should also be noted that, even though the reflectors were not tested at higher power levels due to the lack of sources we had access to, recently an investigation by Angstenberger and co-authors [70] has shown that TPP-fabricated micro-optics are capable of sustaining watt-level of infrared optical power with no signs of degradation, further suggesting that TPP can indeed be applied in applications requiring high power such as those discussed above.

Funding. National Science Foundation (ITE-2236093, NSF ITE Convergence Accelerator); Ministry of Education—Singapore (International Postdoctoral Fellowship).

Acknowledgment. Part of this work was conducted at the shared nanofabrication facilities of MIT.nano and Harvard's Center for Nanoscale Systems (CNS). J.X.B.S. acknowledges financial support from the Ministry of Education—Singapore (International Postdoctoral Fellowship). This work was partially supported by NSF ITE Convergence Accelerator Track I: Building a Sustainable, Innovative Ecosystem for Microchip Manufacturing.

Disclosures. The authors declare no conflicts of interest.

Data Availability. Data underlying the results presented in this paper are not publicly available at this time but may be obtained from the authors upon reasonable request.

REFERENCES

1. N. M. Fahrenkopf, C. McDonough, G. L. Leake, *et al.*, "The AIM photonics MPW: a highly accessible cutting edge technology for rapid prototyping of photonic integrated circuits," IEEE J. Sel. Top. Quantum Electron. **25**, 8201406 (2019).
2. J. X. B. Sia, X. Li, J. Wang, *et al.*, "Wafer-scale demonstration of low-loss (∼0.43 dB/cm), high-bandwidth (>38 GHz), silicon photonics platform operating at the C-band," IEEE Photonics J. **14**, 6628609 (2022).
3. K. Wei, W. Li, H. Tan, *et al.*, "High-speed measurement-device-independent quantum key distribution with integrated silicon photonics," Phys. Rev. X **10**, 031030 (2020).
4. A. Sludds, S. Bandyopadhyay, Z. Chen, *et al.*, "Delocalized photonic deep learning on the internet's edge," Science **378**, 270–276 (2022).
5. Y. Shen, N. C. Harris, S. Skirlo, *et al.*, "Deep learning with coherent nanophotonic circuits," Nat. Photonics **11**, 441–446 (2017).
6. J. Sun, R. Kumar, M. Sakib, *et al.*, "A 128 Gb/s PAM4 silicon microring modulator with integrated thermo-optic resonance tuning," J. Lightwave Technol. **37**, 110–115 (2019).
7. D. M. Kita, B. Miranda, D. Favela, *et al.*, "High-performance and scalable on-chip digital Fourier transform spectroscopy," Nat. Commun. **9**, 4405 (2018).
8. K. Jang, A. Novick, A. Rizzo, *et al.*, "Universal CMOS-foundry compatible platform for ultra-low loss SOI waveguide bends," in *Optical Fiber Communications Conference and Exhibition (OFC)* (Optica, 2023), paper Th3A.5.
9. S. Chung, M. Nakai, and H. Hashemi, "Low-power thermo-optic silicon modulator for large-scale photonic integrated systems," Opt. Express **27**, 13430–13459 (2019).
10. Y. Yuan, Y. Peng, W. Sorin, *et al.*, "A 1 Tbps DWDM microring modulator silicon chip empowered by two-segment Z-shape junctions," Nat. Commun. **15**, 918 (2023).
11. E. Berikaa, M. S. Alam, S. Bernal, *et al.*, "Next-generation O-band coherent transmission for 1.6 Tbps 10 km intra-datacenter interconnects," J. Lightwave Technol. **42**, 1126–1135 (2023).
12. S. Lischke, A. Peczek, J. S. Morgan, *et al.*, "Ultra-fast germanium photodiode with 3-dB bandwidth of 265 GHz," Nat. Photonics **15**, 925–931 (2021).
13. A. H. Atabaki, S. Moazeni, F. Pavanello, *et al.*, "Integrating photonics with silicon nanoelectronics for the next generation of systems on a chip," Nature **556**, 349–354 (2018).
14. C. V. Poulton, M. J. Byrd, P. Russo, *et al.*, "Long-range LiDAR and free-space data communication with high-performance optical phased arrays," IEEE J. Sel. Top. Quantum Electron. **25**, 7700108 (2019).
15. S. Daudlin, A. Rizzo, S. Lee, *et al.*, "3D photonics for ultra-low energy, high bandwidth-density chip data links," arXiv, arXiv:2310.01615 (2023).
16. L. Ranno, Y. Z. Tan, C. S. Ong, *et al.*, "Crown ether decorated silicon photonics for safeguarding against lead poisoning," arXiv, arXiv:2311.07581 (2023).
17. L. Ranno, P. Gupta, K. Gradkowski, *et al.*, "Integrated photonics packaging: challenges and opportunities," ACS Photonics **9**, 3467–3485 (2022).
18. L. Carroll, J.-S. Lee, C. Scarcella, *et al.*, "Photonic packaging: transforming silicon photonic integrated circuits into photonic devices," Appl. Sci. **6**, 426 (2016).
19. R. Marchetti, C. Lacava, L. Carroll, *et al.*, "Coupling strategies for silicon photonics integrated chips [Invited]," Photonics Res. **7**, 201–239 (2019).
20. M. Trappen, M. Blaicher, P.-I. Dietrich, *et al.*, "3D-printed optical probes for wafer-level testing of photonic integrated circuits," Opt. Express **28**, 37996–38007 (2020).
21. R. Polster, L. Y. Dai, O. A. Jimenez, *et al.*, "Wafer-scale high-density edge coupling for high throughput testing of silicon photonics," in *Optical Fiber Communications Conference and Exposition (OFC)* (IEEE, 2018), pp. 1–3.
22. X. Mu, S. Wu, L. Cheng, *et al.*, "Edge couplers in silicon photonic integrated circuits: a review," Appl. Sci. **10**, 1538 (2020).
23. L. Cheng, S. Mao, Z. Li, *et al.*, "Grating couplers on silicon photonics: design principles, emerging trends and practical issues," Micromachines **11**, 666 (2020).
24. R. S. Tummidi and M. Webster, "Multilayer silicon nitride-based coupler integrated into a silicon photonics platform with <1 dB coupling loss to a standard SMF over O, S, C and L optical bands," in *Optical Fiber Communications Conference and Exhibition (OFC)* (Optica, 2020) paper Th2A.10.
25. Y. Ding, C. Peucheret, H. Ou, *et al.*, "Fully etched apodized grating coupler on the SOI platform with −0.58 dB coupling efficiency," Opt. Lett. **39**, 5348–5350 (2014).
26. L. Ranno, J. X. B. Sia, K. P. Dao, *et al.*, "Multi-material heterogeneous integration on a 3-D photonic-CMOS platform," Opt. Mater. Express **13**, 2711–2725 (2023).
27. P.-I. Dietrich, M. Blaicher, I. Reuter, *et al.*, "*In situ* 3D nanoprinting of free-form coupling elements for hybrid photonic integration," Nat. Photonics **12**, 241–247 (2018).
28. S. Yu, Q. Du, C. R. Mendonca, *et al.*, "Two-photon lithography for integrated photonic packaging," Light Adv. Manuf. **4**, 32 (2023).
29. H. Wang, W. Zhang, D. Ladika, *et al.*, "Two-photon polymerization lithography for optics and photonics: fundamentals, materials, technologies, and applications," Adv. Funct. Mater. **33**, 2214211 (2023).
30. O. A. Jimenez Gordillo, S. Chaitanya, Y.-C. Chang, *et al.*, "Plug-and-play fiber to waveguide connector," Opt. Express **27**, 20305–20310 (2019).
31. C. Wan, J. L. Gonzalez, T. Fan, *et al.*, "Fiber-interconnect silicon chiplet technology for self-aligned fiber-to-chip assembly," IEEE Photonics Technol. Lett. **31**, 1311–1314 (2019).

32. S. Yu, T. K. Gaylord, and M. S. Bakir, "Fiber-array-to-chip interconnections with sub-micron placement accuracy via self-aligning chiplets," IEEE Photonics Technol. Lett. **34**, 1023–1025 (2022).
33. S. Yu, T. K. Gaylord, and M. S. Bakir, "Scalable fiber-array-to-chip interconnections with sub-micron alignment accuracy," in *IEEE 73rd Electronic Components and Technology Conference (ECTC)* (IEEE, 2023), pp. 748–752.
34. https://www.phix.com/phix-partners-nanoscribe-microlenses/.
35. N. Lindenmann, G. Balthasar, D. Hillerkuss, *et al.*, "Photonic wire bonding: a novel concept for chip-scale interconnects," Opt. Express **20**, 17667–17677 (2012).
36. H.-W. Rhee, J. Shim, J.-Y. Kim, *et al.*, "Direct optical wire bonding through open-to-air polymerization for silicon photonic chips," Opt. Lett. **47**, 714–717 (2022).
37. M. Blaicher, M. R. Billah, J. Kemal, *et al.*, "Hybrid multi-chip assembly of optical communication engines by *in situ* 3D nano-lithography," Light Sci. Appl. **9**, 71 (2020).
38. M. R. Billah, M. Blaicher, T. Hoose, *et al.*, "Hybrid integration of silicon photonics circuits and InP lasers by photonic wire bonding," Optica **5**, 876–883 (2018).
39. S. Yu, J. Lu, V. Ginis, *et al.*, "On-chip optical tweezers based on freeform optics," Optica **8**, 409–414 (2021).
40. S. Singer, Y. Xu, S. T. Skacel, *et al.*, "3D-printed facet-attached optical elements for beam shaping in optical phased arrays," Opt. Express **30**, 46564–46574 (2022).
41. N. Lindenmann, *Photonic Wire Bonding as a Novel Technology for Photonic Chip Interfaces* (Karlsruhe Institute of Technology, 2018).
42. N. Lindenmann, S. Dottermusch, M. L. Goedecke, *et al.*, "Connecting silicon photonic circuits to multicore fibers by photonic wire bonding," J. Lightwave Technol. **33**, 755–760 (2015).
43. H. Luo, F. Xie, Y. Cao, *et al.*, "Low-loss and broadband fiber-to-chip coupler by 3D fabrication on a silicon photonic platform," Opt. Lett. **45**, 1236–1239 (2020).
44. H. Luo, L. Chen, S. Yu, *et al.*, "Efficient four-way vertical coupler array for chip-scale space-division-multiplexing applications," Opt. Lett. **46**, 4324–4327 (2021).
45. S. Yu, L. Ranno, Q. Du, *et al.*, "Free-form micro-optics enabling ultrabroadband low-loss off-chip coupling," Laser Photonics Rev. **17**, 2200025 (2023).
46. https://www.eeweb.com/lead-free-solder-reflow-for-semiconductor-power-devices/.
47. A. Rizzo, A. Novick, V. Gopal, *et al.*, "Massively scalable Kerr comb-driven silicon photonic link," Nat. Photonics **17**, 781–790 (2023).
48. L. Tombez, E. J. Zhang, J. S. Orcutt, *et al.*, "Methane absorption spectroscopy on a silicon photonic chip," Optica **4**, 1322–1325 (2017).
49. J. Park, S. Kim, D. W. Nam, *et al.*, "Free-form optimization of nanophotonic devices: from classical methods to deep learning," Nanophotonics **11**, 1809–1845 (2022).
50. R. Marchetti, C. Lacava, A. Khokhar, *et al.*, "High-efficiency grating-couplers: demonstration of a new design strategy," Sci. Rep. **7**, 16670 (2017).
51. Z. Hou, X. Li, Y. Huang, *et al.*, "Physics of elliptical reflectors at large reflection and divergence angles II: analysis of optical beam distortions in integrated ultra-large-angle elliptical curved reflectors," Opt. Commun. **287**, 106–116 (2013).
52. M. Schmid, D. Ludescher, and H. Giessen, "Optical properties of photoresists for femtosecond 3D printing: refractive index, extinction, luminescence-dose dependence, aging, heat treatment and comparison between 1-photon and 2-photon exposure," Opt. Mater. Express **9**, 4564–4577 (2019).
53. B. Snyder and P. O'Brien, "Planar fiber packaging method for silicon photonic integrated circuits," in *Optical Fiber Communications Conference and Exposition (OFC)* (IEEE, 2012), paper OM2E.5.
54. S. Yu, H. Zuo, X. Sun, *et al.*, "Optical free-form couplers for high-density integrated photonics (OFFCHIP): a universal optical interface," J. Lightwave Technol. **38**, 3358–3365 (2020).
55. https://www.nanoscribe.com/en/products/quantum-x-align/.
56. J. Zou, Y. Zhang, J. Hu, *et al.*, "Grating coupler with reduced back reflection using $\lambda/4$ offset at its grating sub-teeth," J. Lightwave Technol. **37**, 1195–1199 (2019).
57. G. Georgieva, K. Voigt, A. Peczek, *et al.*, "Design and performance analysis of integrated focusing grating couplers for the transverse-magnetic TM_{00} mode in a photonic BiCMOS technology," J. Eur. Opt. Soc. Rapid Publ. **16**, 7 (2020).
58. S. Romero-Garcia, B. Marzban, F. Merget, *et al.*, "Edge couplers with relaxed alignment tolerance for pick-and-place hybrid integration of III–V lasers with SOI waveguides," IEEE J. Sel. Top. Quantum Electron. **20**, 369–379 (2014).
59. https://mrsisystems.com/mrsi-s-hvm/.
60. H. Gehring, M. Blaicher, W. Hartmann, *et al.*, "Low-loss fiber-to-chip couplers with ultrawide optical bandwidth," APL Photonics **4**, 010801 (2019).
61. P. Gruber, "Method for the lithography-based additive manufacturing of a three-dimensional component," U.S. patent US11787106B2 (October 17, 2023).
62. https://www.nanoscribe.com/en/products/quantum-x/.
63. L. Ranno, T. Gu, and J. Hu, "Integrated freeform optical couplers and fabrication methods thereof," U.S. patent US20230393357A1 (June 5, 2023).
64. F. Cantoni, D. Maher, E. Bosler, *et al.*, "Round-robin testing of commercial two-photon polymerization 3D printers," Addit. Manuf. **76**, 103761 (2023).
65. https://www.upnano.at/technology/#process.
66. J. Purtov, A. Verch, P. Rogin, *et al.*, "Improved development procedure to enhance the stability of microstructures created by two-photon polymerization," Microelectron. Eng. **194**, 45–50 (2018).
67. J. Riemensberger, N. Kuznetsov, J. Liu, *et al.*, "A photonic integrated continuous-travelling-wave parametric amplifier," Nature **612**, 56–61 (2022).
68. B. Wang, J. S. Morgan, K. Sun, *et al.*, "Towards high-power, high-coherence, integrated photonic mmWave platform with microcavity solitons," Light Sci. Appl. **10**, 4 (2021).
69. C. V. Poulton, M. J. Byrd, P. Russo, *et al.*, "Coherent LiDAR with an 8,192-element optical phased array and driving laser," IEEE J. Sel. Top. Quantum Electron. **28**, 6100508 (2022).
70. S. Angstenberger, P. Ruchka, M. Hentschel, *et al.*, "Hybrid fiber–solid-state laser with 3D-printed intracavity lenses," Opt. Lett. **48**, 6549–6552 (2023).